Halloysite nanotube-magnetic iron oxide nanoparticle hybrids for the rapid catalytic decomposition of pentachlorophenol

Tsoufis, T.; Katsaros, F.; Kooi, B. J.; Bletsa, E.; Papageorgiou, S.; Deligiannakis, Y.; Panagiotopoulos, I.

Published in:
Chemical Engineering Journal

DOI:
10.1016/j.cej.2016.12.056

Publication date:
2017

Chemical Engineering Journal 313 (2017) 466–474

Contents lists available at ScienceDirect

Chemical Engineering Journal

journal homepage: www.elsevier.com/locate/cej

Halloysite nanotube-magnetic iron oxide nanoparticle hybrids for the rapid catalytic decomposition of pentachlorophenol

T. Tsoufis [a,*], F. Katsaros [a], B.J. Kooi [b], E. Bletsa [c], S. Papageorgiou [a], Y. Deligiannakis [c], I. Panagiotopoulos [d]

[a] N.C.S.R. "Demokritos", Institute of Nanoscience & Nanotechnology, GR15310 Athens, Greece
[b] Zernike Institute for Advanced Materials and Materials Innovation Institute M2i, University of Groningen, NL9747AG Groningen, The Netherlands
[c] Department of Physics, University of Ioannina, GR45110 Ioannina, Greece
[d] Department of Materials Science & Engineering, University of Ioannina, GR45110 Ioannina, Greece

HIGHLIGHTS

- *In situ* growth of small magnetite nanoparticles at natural clay nanotubes (halloysite).
- Novel, facile synthetic strategy involving a modified wet-impregnation method.
- Efficient catalytic decomposition of pentachlorophenol by magnetite@halloysite hybrids.
- Catalytic efficiency of hybrids significant higher compared to free nanoparticles.
- Hybrids can be reused for multiple catalytic cycles without noteworthy loss of activity.

GRAPHICAL ABSTRACT

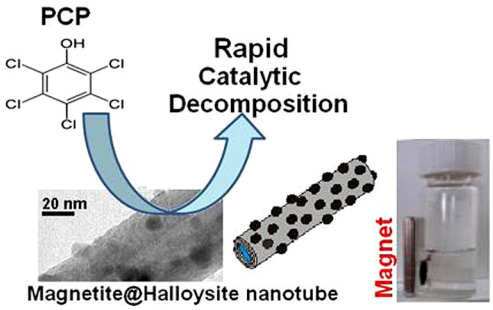

ARTICLE INFO

Article history:
Received 26 August 2016
Received in revised form 13 December 2016
Accepted 14 December 2016
Available online 18 December 2016

Keywords:
Clay nanotubes
Magnetite nanoparticle
Magnetite/halloysite hybrids
Catalytic decomposition of pentachlorophenol
Magnetic separation
Reuse of catalytic hybrids

ABSTRACT

Halloysite clay are a very attractive class of alumino-silicate based, natural nanotubes possessing high-aspect ratio, significant thermal and mechanical stability, as well as tunable surface chemistry. We report a novel, facile, synthetic approach involving a modified wet-impregnation method for the *in situ* synthesis of small, magnetite nanoparticles at the surface of natural halloysite nanotubes. In addition to their magnetic properties, the synthesized magnetite-halloysite hybrids are evaluated for the first time against the catalytic decomposition of pentachlorophenol from reaction solutions at room temperature. Their performance was found superior compared to free, self-supported NPs synthesized with previously reported methods. Very interestingly, after their first catalytic evaluation cycle and because of their magnetic properties the hybrids could be easily recovered from their corresponding reaction solution. The halloysite-nanoparticle hybrids are also very promising in terms of sustainability, since we demonstrate that they can be re-collected, cleaned and re-used for multiple catalytic cycles without any significant loss in their catalytic activity.

1. Introduction

Halloysite clay nanotubes (denoted hereafter as *HNT*) comprises of naturally occurring aluminosilicate nanotubes with a 1:1 Al:Si ratio and a stoichiometry of $Al_2Si_2O_5(OH)_4{\cdot}nH_2O$ [1]. HNT contain octahedral gibbsite $Al(OH)_3$ and tetrahedral SiO_4 sheets in the form

* Corresponding author.
E-mail address: t.tsoufis@inn.demokritos.gr (T. Tsoufis).

http://dx.doi.org/10.1016/j.cej.2016.12.056
1385-8947/

of hollow cylinders formed by multiply rolled layers [2]. Due to their nanotubular shape, HNT possess highly meso-/macro-scopic pore structure and large specific surface area. Moreover, their hollow tubular morphology provides a confined space to host guest species (i.e. radicals, drugs or metal nanoparticles), which after their immobilization within the hollow cavity of HNT, are accessible to gas and liquids and thus can participate into targeted chemical reactions (i.e. such as catalysis). In addition, HNT exhibit a well-defined and tunable surface chemistry, are far less expensive compared to other types of nanotubes (i.e. carbon nanotubes), are abundantly available (global annual supply is estimated to over 50.000 tons), while due to their aluminosilicate structure, they are durable exhibiting high mechanical strength and thermal stability. Most importantly and in contrast to other types of nanotubes, HNT are biocompatible (non-toxic) [1,3–5], making their use suitable in environment-related applications. Therefore, HNT are extremely robust and attractive as support for active phases in the field of environmental catalysis [6,7].

Pentachlorophenol (denoted hereafter as *PCP*) is a highly recalcitrant chlorinated organic compound found extensively in surface and ground aquatic systems as well as in soils. The main source of PCP contamination originates from the industry and agriculture, where it is used as insecticide, biocide, herbicide, pesticide and wood preservative. U.S. Environmental Protection Agency classifies PCP as model pollutant due to its high toxicity (PCP exhibits specific organ toxicity towards liver, kidneys and the central nervous system) as well as its' resistance to degradation [8–11]. Since PCP biodegrades very slowly, various remediation techniques are required for its removal. Among them, heterogeneous supported catalysts offer advantages versus non-supported catalysts since their immobilization increases the stability of the active catalytic phase and prevents oxidative degradation by bimolecular interaction [8,12]. During the last decade, magnetically separable catalysts and their use in heterogeneous catalytic reactions became very promising and attracted significant interest. Magnetic nanoparticles as catalysts offer advantages as they are easily separable and recyclable [13]. Among these catalysts, iron oxide nanoparticles, such as magnetite (Fe_3O_4), are capable of decomposing recalcitrant organic contaminants, providing a promising alternative for the oxidative treatment of polluted soil and water [14,15].

Following the constantly increasing interest on HNT, the field of metal nanoparticle-HNT hybrids is established as a research area with potential applications in diverse fields including sensors [16–19], catalysts [7,20–22], and coatings [23–25]. Various types of metal nanoparticles (denoted hereafter as NPs) including palladium, gold, silver and copper NPs have been synthesized or immobilized at the outer surface or inside the hollow cavity of HNT [7,17,26,27]. Despite the increasing interest in the field of NPs/HNT hybrids, the volume of reported studies on iron oxide NPs/HNT hybrids in particular, remains very limited, and up-to-date involves either the development of polymer/carbon coated NPs@HNT composites [28,29] or the development of very large assemblies of NPs at the surface of HNT developed by the Fe^{2+}/Fe^{+3} coprecipitation method [30–32]. However, the use of the so-called "coprecipitation" method offers very limited control of particle size [33,34], as only kinetic factors are governing the growth of the crystal. This drawback is also observed in the heavily aggregated magnetite NPs assemblies (with size of several dozens of nm) developed on HNT using this approach [30–32]. Moreover, and despite the increasing research focus on halloysite clay nanotubes for environment-related applications [6,7,35], to the best of our knowledge there has not been any literature report involving the use of HNT and/or magnetite NPs/HNT hybrids for the catalytic decomposition of pentachlorophenol.

In our study we report the *in situ* synthesis of relatively small, magnetite NPs dispersed along the surface of HNT by a novel, facile approach involving a modified wet-impregnation method previously successfully employed for the development of magnetite NPs at various porous substrates [36–39]. The synthetic methodology includes the immobilization of the iron cations at the HNT's surface, followed by interaction with acetic acid vapors and calcination. Our methodology does not require the separate synthesis of metal NPs, and therefore avoids the extra synthetic steps required to connect pre-formed metal NPs with HNT. In terms of employing HNT as template for the development of hybrids useful in catalytic applications, halloysite clays are very attractive, natural-occurring, low-cost, nano-structured candidates since (i) pristine HNT bear active, surface silanol groups that could act as anchoring sites for the iron cations (NPs precursor) leading to the covalent attachment of the resulting iron oxide NPs, thus minimizing undesirable leaching phenomena in liquid phase catalysis, and (ii) HNT are redox-inert, thus during the oxidative catalytic reactions the HNT substrate will be not hampered. Furthermore, the use of HNT as one-dimensional support, hinders the extensive aggregation of the formed iron oxide NPs to large, heavily aggregated assemblies (as observed in the case of self-supported NPs) enhancing the overall catalytic performance of the iron oxide/HNT hybrids The starting materials, their intermediate derivatives, and the final products were studied with a combination of experimental methods including X-ray diffraction (XRD), electron microscopy (SEM, TEM), and spectroscopy (FT-IR, XPS) techniques. Furthermore, the magnetic properties of the synthesized hybrids were thoroughly studied in-depth at different temperatures (from 290 K to 77 K) employing magnetic (VSM) measurements. The performance of synthesized NPs@HNT hybrids was evaluated for the first time against the catalytic decomposition of PCP with the obtained results highlighting their excellent catalytic activity towards the rapid and efficient catalytic degradation PCP at room temperature. In addition, we demonstrate that following their first catalytic evaluation cycle the NPs@HNT hybrids can be separated from their corresponding reaction mixture by simply applying an external magnetic field (i.e. magnet), cleaned and re-used for additional multiple catalytic cycles without any significant loss of their catalytic activity.

2. Experimental

2.1. Reagents and instrumentation

Halloysite clay was purchased from Sigma-Aldrich and was sieved before use to eliminate larger aggregates. All chemical reagents were used as purchased without any further purification. Iron nitrate nonahydrate, PCP, sodium periodate and acetic acid (99.7%) were purchased from Sigma-Aldrich while ethanol (99.5%), methanol (99.8%), acetone (99.95%) and acetonitrile were purchased from Fischer Scientific. All relative details regarding the employed instrumentation are provided in the Supplementary Data section.

2.2. Synthesis of NPs@HNT hybrids and self-supported NPs

The NPs@HNT hybrids were prepared based on a modified wet impregnation method we have previously employed for developing magnetite NPs on carbon-based supports [36,37]. In brief, the synthetic methodology involved the dispersion of a certain quantity of purified HNT in 50 ml CH_3OH containing a quantity of Fe $(NO_3)_3{\cdot}9H_2O$ (100 mg) to yield hybrid samples containing 17% wt. iron. The mixture was further stirred for 18 h, followed by rapid removal of the solvent at 80 °C. The as-prepared powder was

exposed to vapors of acetic acid (99.5%) at 80 °C for 60 min. The obtained sample was further dried for 15 min at 80 °C in order to remove any physically absorbed acetic acid. The final NPs@HNT hybrids were obtained by calcination for 1 h at 200 °C under high-purity argon flow (100 sccm, 99.999%). The synthesis of free magnetite nanoparticles (employed for comparison purposes) is discussed in the Supplementary Data section.

2.3. Catalytic decomposition of PCP

The catalytic reactions were performed in test tubes of 4 mL volume at room temperature, without a magnetic stirrer i.e. the reaction mixture was shaken on a rotary shaker. A typical reaction mixture containing 5 mg of the NPs@HNT hybrids, 30 μM PCP (300 μL of a 200 μM PCP stock solution in CH_3CN) and 225 μM of the $NaIO_4$ oxidant (30 μL of a 15 mM $NaIO_4$ aqueous stock solution). For all evaluated reactions, the final volume of the reaction was 2 mL of acetonitrile. Acetonitrile was used as solvent with the double purpose of (i) eliminating side reactions that would oxidize the iron atoms, and (ii) fully solubilize the hydrophobic PCP. The amount of H_2O used herein, in the addition of oxidant was 10^{-3}% of the reaction volume. The quantification of PCP by HPLC was based on comparison with standards. In addition, 2 mg of free unsupported magnetite NPs were also evaluated under the same catalytic conditions as reference sample. In this catalytic protocol the initial solution potential was 381 mV vs. Standard Hydrogen Electrode (SHE), calibrated by a 10 mM/10 mM aqueous solution of $K_3Fe(CN)_6/K_2Fe(CN)_6$ (Eh reference = 236 mV).

2.4. Recycling

After the first use of the nanohybrids, the solid powder was separated by the use of a magnet, and it was next washed using acetonitrile according to the following procedure: 4 ml of acetonitrile was added to the catalyst and sonicated for 10 min. The mixture was centrifuged, and the solvent was removed. This procedure was repeated three times. The solid sediment was dried at room temperature, collected in the form of fine powder and reused according to the procedure described above.

3. Results and discussion

3.1. Characterization of NPs@HNT hybrids

A schematic overview of the employed methodology is presented in Scheme 1. Pristine HNT consist of gibbsite octahedral sheet (Al–OH) groups on their internal surface and siloxane groups (Si–O–Si) on their external surface. This difference results in a negatively charged outer surface and a positively charged inner lumen in pH < 8.5 [3]. The concept of our approach involved the immobilization of the positively charged NPs precursor (iron cations) mainly at the outer surface of HNT. At the next step of synthesis, the system was exposed to acid acetic vapor. Acetic acid vapors show very high affinity to react with iron cations to form iron acetate precursor species [37,38]. Those intermediate species yield the final small, magnetic nanoparticles upon heating. Due to the successful dispersion and stabilization of the iron species on the HNT, the appearance of the intermediate derivative changed from deep white for the pristine material (Scheme 1a, top) to dark orange (Scheme 1b, top). The final NPs@HNT hybrids were developed upon pyrolysis under inert (Ar) atmosphere (Scheme 1c).

FT-IR spectroscopy was employed to monitor the intermediate products during the various steps of the synthetic procedure. In particular, the spectrum of pristine HNT (Fig. 1a) shows a set of major bands at the low frequency region recorded at 458, 526, 746, 794, and 905 cm^{-1} corresponding respectively at Si–O deformation, Al–O–Si deformation, perpendicular Si–O stretching, symmetric Si–O stretching and inner O–H deformations [40]. Additional bands were recorded at 1.010 (followed by a secondary at 1.116), 1.648, 3.620 and 3.691 cm^{-1} attributed to in-plane Si–O stretching, O–H deformation of water, inner O–H stretching and inner surface O–H stretching correspondingly [1]. The IR spectrum of the intermediate HNT + Fe derivative after the modified wet impregnation step with iron nitrate solution (Fig. 1b), exhibited the same set of vibration bands followed by the clear appearance of additional bands at 1.348 and 1.395 cm^{-1} not recorded in the corresponding spectrum of pristine HNT. Those additional peaks are due to the presence of nitrate anions (originating from NPs precursor) which remained after drying, and they are attributed to asymmetric NO_3^- vibrations [39]. Moreover in the same spectrum, the recorded increase in the intensity of the broad band at 668 cm^{-1} is assigned to the presence of iron groups. Further changes were observed in the IR spectrum of the HNT + Fe derivative after exposure to acetic acid vapors (Fig. 1c). The characteristic O—C=O deformation band originating from acetic acid was evidenced at 657 cm^{-1} [41], confirming the successful attachment of acetic acid at the HNT-Fe precursor system. The newly-appeared, strong bands at 1.585 and 1.444 cm^{-1} are assigned to asymmetric and symmetric vibrations respectively of COO^- species (originating from acetic acid) bridged to Fe(III) due to formation of a trinuclear Fe^{3+} complex [42].

SEM images of pristine material (Suppl. Data, Fig. S1) showed a typical HNT morphology exhibiting a hollow tubular structure with both ends open. The length of individual HNT ranged from 500 to 1.000 nm, while the diameter of the inner lumen varied from 15 to 30 nm. High resolution TEM images (Suppl. Data, Fig. S2) indicate that the thicknesses of the crystalline aluminosilicate HNT wall fall within the range of 10–15 nm. Electron

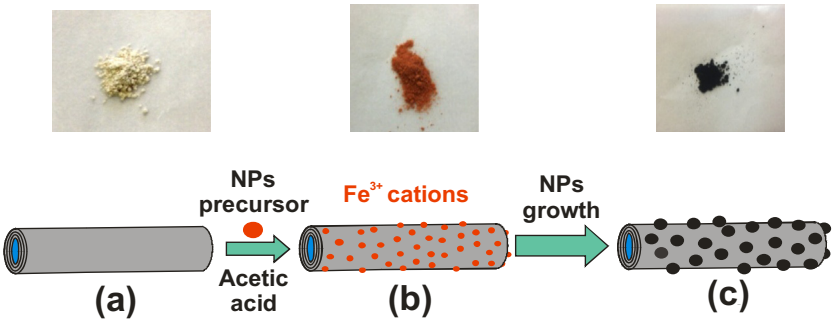

Scheme 1. Schematic overview of the synthetic strategy for the development of NPs@HNT (bottom) and corresponding digital images of the starting, intermediate and final materials (top).

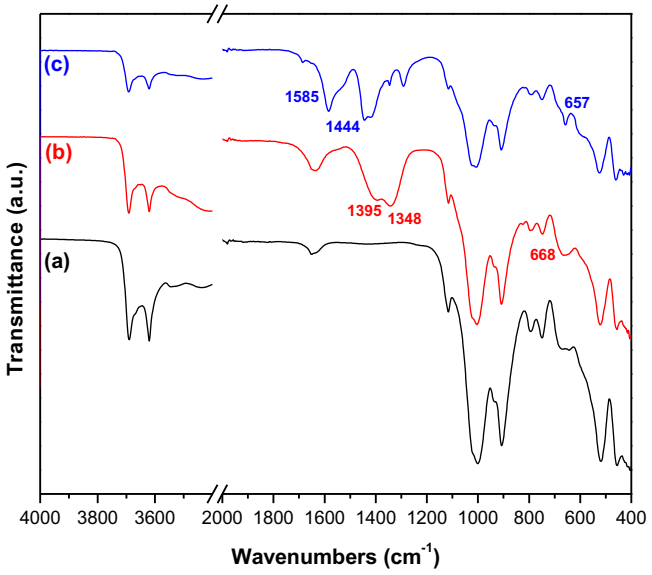

Fig. 1. FT-IR spectra of pristine HNT (a), and HNT + Fe (b), HNT + Fe + Acetic acid (c) derivatives.

microscopy images of the synthesized NPs@HNT hybrids confirmed the successful development of NPs attached at the surface of HNT (Figs. 2 and 3 and Fig. S3 – Suppl. Data). The TEM study showed that HNT retained their tubular morphology during NPs synthesis and confirmed the development of rather uniform and relatively small in size NPs dispersed along HNT surfaces without any significant accumulation into larger assemblies. Based on a statistical analysis of the acquired TEM images, the average size of the synthesized NPs was estimated to be about 15(±4) nm. High resolution TEM images confirmed the successful development of NPs and in addition confirmed their intrinsic crystallography (Fig. 3). The planar space of 0.24 marked in Fig. 3b-insert is typically reported as the (3 1 1) spacing plane of magnetite nanocrystals [43,44].

The XRD pattern of the final NPs@HNT hybrids (Fig. 4b) shows all the characteristic HNT diffraction peaks also recorded for starting HNT (Fig. 4a) without any noticeable change in neither their relative intensities nor their relative 2θ values. This finding suggests that HNT in the final hybrids retained the overall tube-wall crystallinity of the starting material as previously reported after thermal treatment of HNT samples at similar temperature [6,45]. The XRD pattern of starting HNT (Fig. 4a) closely resembled the corresponding pattern of pristine HNT (JCPDS # 29-1487) [7,46]. In particular, it showed a sharp 001 diffraction peak at 11.9° due to the multilayer HNT wall packing (corresponding to a basal spacing of 0.73 nm) and indicating a dehydrated HNT structure. The strong 0 0 1 diffraction was followed by the appearance of the characteristic ⟨0 2 0⟩, ⟨0 0 2⟩, ⟨1 3 0⟩, ⟨1 3 1⟩,⟨0 0 3⟩, ⟨2 0 3⟩ set of diffraction peaks recorded at 2θ values ~20°, 24.6°, 34.9°, 35.8°, 38.2° and 45.5° correspondingly [1,47–49]. The diffraction peaks recorded at $2\theta \approx 18.2°$ (followed by a weaker diffraction peak at ~29.5°) and ~26° are respectively attributed to the co-presence of the gibbsite (JCPDS # 33-0018) and quartz (JCPDS # 46-1045) mineral phases which are commonly reported to co-exist among HNT deposits [50,51] since all three minerals are formed under similar geological conditions [52,53]. Nevertheless, the latter non-HNT phases are only minor in content since the extensive SEM and TEM study of the starting material (discussed above) revealed that the presence of HNT is dominant among the starting material. In addition, it is worth highlighting that in the XRD pattern of NPs@HNT (Fig. 4b), the 2θ position of the strong 0 0 1 diffraction peak, did not shift compared to pristine HNT. This finding suggests that the NPs precursor and the subsequently synthesized NPs were deposited solely at the surface of HNT rather than intercalated between the interlayer wall-spacings. The recorded XRD pattern of NPs@HNT (Fig. 4b) was very similar to the corresponding pattern of the starting HNT. The key reason is that the main characteristic diffraction peaks of the synthesized iron-rich phase are expected within the 2θ range 30–40°, and thus overlap with the much sharper diffraction peaks of pristine HNT recorded in the same 2θ region (Fig. 4a). This extended overlapping of the HNT and NPs diffraction peaks does not allow safe conclusions regarding the type of synthesized iron oxide crystalline phase exclusively by XRD. Nevertheless, it is worth highlighting an observed broadening in the pattern of NPs@HNT at $2\theta \sim 35°$, probably due to contribution from the ⟨3 1 1⟩ diffraction peak of the synthesized iron oxide phase expected at the same 2θ range (JCPDS cards in Fig. 4). A secondary reason for the observed profile of the NPs@HNT's pattern (Fig. 4b), is due to smearing out of the NPs

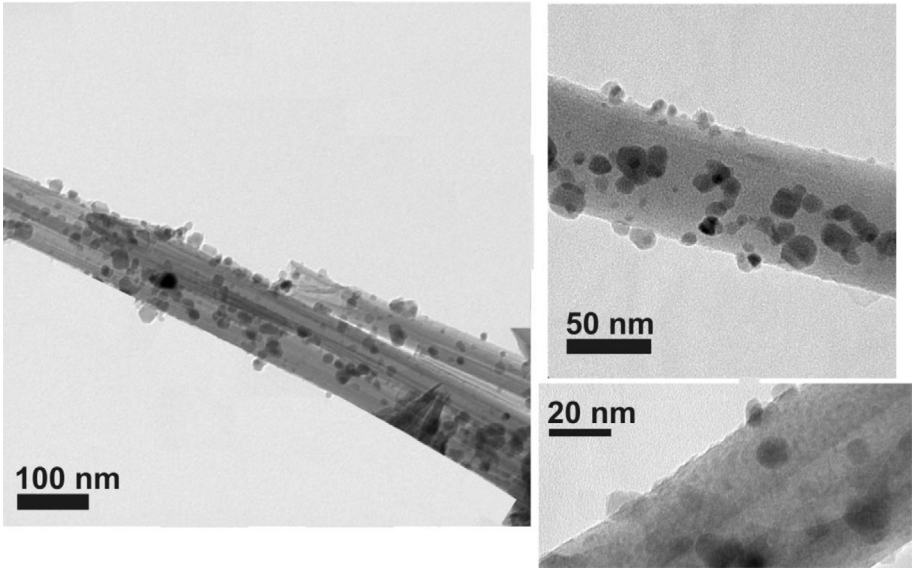

Fig. 2. TEM images of NPs@HNT hybrids.

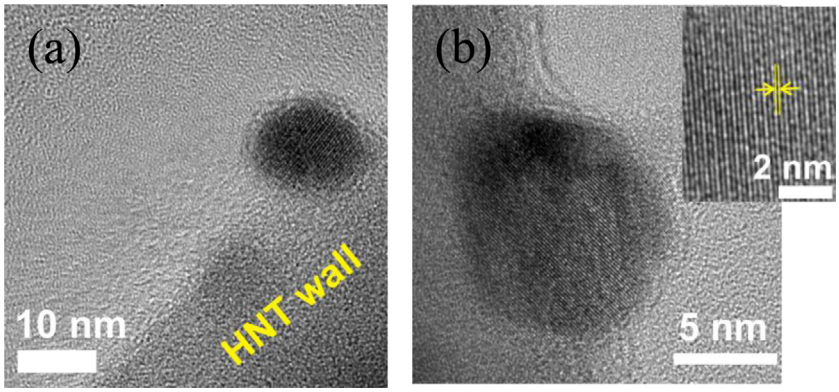

Fig. 3. High-resolution TEM images of synthesized NPs at HNT (a, b) and their corresponding crystalline planar planes (b, insert).

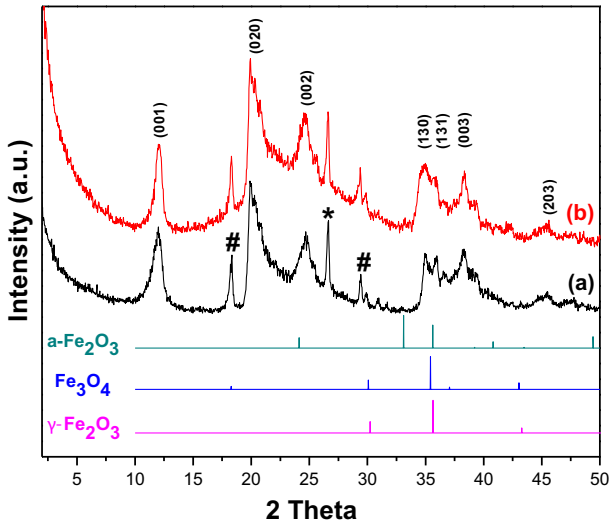

Fig. 4. XRD patterns of starting HNT (a) and NPs@HNT (b) hybrids. Symbols # and * correspond to gibbsite and quartz phases respectively. The diffraction patterns of α-Fe_2O_3 (JCPDS 46-1312), Fe_3O_4 (JCPDS 19-629) and γ-Fe_2O_3 (JCPDS 39-1346) are also shown for comparison.

characteristic diffraction peaks because of their small size as well as their dispersion along the HNT's surface, as evidenced by the TEM study discussed in-detail above. It is worth highlighting that similar observations were also reported in previous studies where small (similarly-sized) NPs were finely dispersed at various substrates, clearly pointing-out that for those NPs the characteristic XRD peaks of their crystalline phases are broad and of low intensity [37,54,55]. The unarguable identification of the synthesized iron oxide nanoparticles' stoichiometry was performed by a thorough study of the high-resolution Fe 2*p* XPS spectrum for NPs@HNT (discussed in detail vide infra).

X-ray photoelectron spectroscopy is a powerful tool for the direct determination of the surface elemental composition. The recorded XPS survey spectra of the starting HNT and the final NPs@HNT hybrids are presented in Fig. 5. Both spectra show the characteristic O 1*s*, C 1*s*, Si 2*s*, Al 2*p*, Si 2*p*, Al 2*p* contributions at 535, 285, 153, 119, 103 and 75 eV binding energies respectively, originating from the HNT aluminosilicate structure. The corresponding survey spectra are presented in Fig. 5b in higher magnification where all relative Si and Al contributions are clearly observed. In the spectrum of the final NPs@HNT (Fig. 5a-ii), one additional peak at ~ 710 eV was recorded. This peak is characteristic of the Fe 2*p* contribution, and was not recorded in the corresponding spectrum of the starting HNT (Fig. 5a–i). The appearance of the Fe 2*p* contribution is further confirming the successful development of the iron oxide NPs on the surface of HNT.

X-ray photoelectron spectroscopy is widely used to confirm the identity of Fe_3O_4 (magnetite) due to its sensitivity towards Fe^{2+} and Fe^{3+} cations [43,56,57]. The high-resolution Fe 2*p* region of the XPS spectrum for NPs@HNT is presented in Fig. 6. The spectrum exhibits the characteristic Fe $2p_{1/2}$ and Fe $2p_{3/2}$ contributions at 711.7 and 724.9 eV, respectively. The profile of the spectrum perfectly resembles published spectra of Fe_3O_4 [58,59]. Those features, together with the absence of the charge transfer satellite of Fe $2p_{3/2}$ at 720 eV characteristic for γ-Fe_2O_3 [60,61] points to the conclusion that the dominant phase in the synthesized NPs@HNT is magnetite.

XPS was also employed to study the interactions of the synthesized magnetite NPs and the HNT support in the final hybrids. The high-resolution Si 2*p* spectra of starting HNT and the final hybrids are presented in Fig. S4 (Suppl. Data). In particular, the spectrum of the starting HNT (Fig. S4i) was fitted using two components. The peak centered at 103.5 eV (corresponding to the 55% of the Si 2*p* intensity) is attributed to the surface silanol groups (Si–OH) of HNT [7]. The second peak centered at 102.7 eV (holding the 45% of the overall intensity) is attributed to the Si–O bonds of the HNT's aluminosilicate framework [62]. The profile of the corresponding high-resolution XPS spectrum for the final NP@HNT hybrids showed significant differences (Fig. S4ii). In particular, the percentage of Si–OH bonds recorded at 103.5 eV was found decreased at 29% of the overall Si 2*p* intensity. The percentage of Si–O bonds recorded at 102.7 eV remained the same at 44%. A third peak corresponding to 27% of the overall Si 2*p* intensity was recorded at 119.6 eV and is attributed to silicon-iron interactions [63]. This latter peak (119.6 eV) confirms the successful attachment of the synthesized magnetite NPs directly at the Si-rich surface of HNT.

The magnetic measurements of the final NPs@HNT performed via VSM are shown in Fig. S5 (Suppl. Data) The magnetic nanoparticles show ferromagnetic behavior and retain a small coercivity up to room temperature although the critical size for superparamagnetic behavior is 25 nm for magnetite and 35 nm for maghemite. The temperature dependence of coercivity very well follows the law expected for single domain fine particles with H_C = 340 Oe and T_B = 530 K. Similarly the remanent magnetization falls linearly, extrapolating to T_B = 520 K. Therefore although the existence of a fraction of smaller particles that are in the superparamagnetic state cannot be excluded, the overall magnetic response is dominated by blocked coercive particles. For instance the magnetization curves measured at different temperatures do not superimpose when plotted against H/T. Although the magnetic response and coercivity are expected to be dominated by the larger

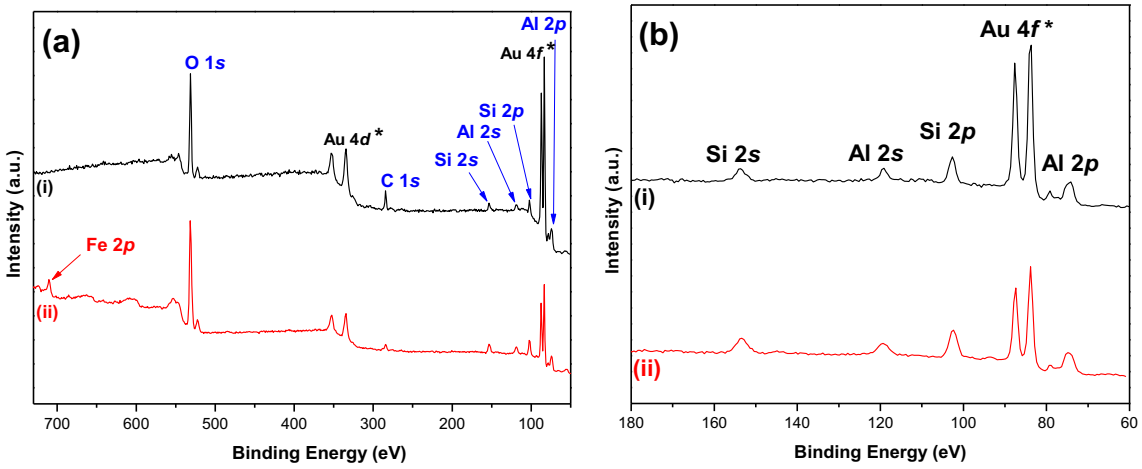

Fig. 5. Survey XPS core level regions of pristine HNT (i) and NPs@HNT hybrids (ii) recorded for samples deposited on gold substrates. Contributions from gold substrate are indicated with an asterisk (∗).

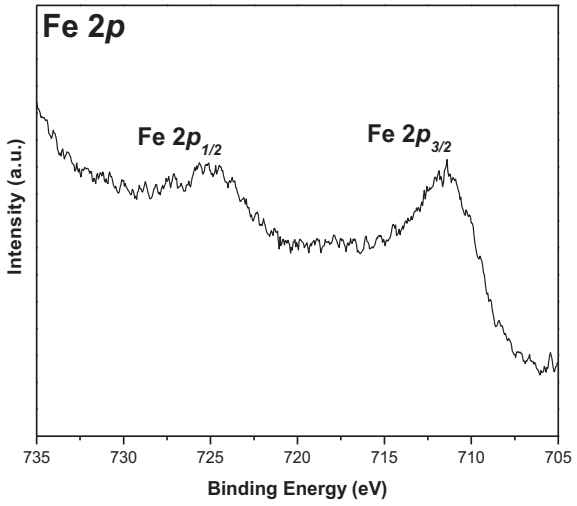

Fig. 6. High resolution Fe 2*p* core level region of the XPS spectrum for NPs@HNT hybrids.

volume particles anyway, the blocking temperature seems high for the average particle size $D = (15 \pm 5)$ nm derived by the TEM studies. The increased T_B can be attributed to the fact that the particles are not completely spherical but have average aspect ratio $a = (1.2 \pm 0.2)$, which means that a shape anisotropy contribution of the order $(1/2)(N_{\perp} - N_{//})M_S^2 \approx 1.2 \times 10^5$ erg/cm^3 has to be added [64] to the magnetocrystalline anisotropy (1.3×10^5 erg/cm^3) of magnetite. For $\alpha = 1.4$ the $T_B = 530$ K can be obtained by a diameter D = 22 nm, compared to D = 30 nm for spherical particles. Surface anisotropy is another possible contribution to the total anisotropy especially on capping-free NPs surfaces [65]. Inter-particle interactions due to particle agglomeration, are not likely to contribute to the T_B increase since the TEM images show that the particles do not form large aggregated assemblies. Furthermore from the measurements of magnetization relaxation with time, a fluctuation field of $H_f = 10$ Oe at 77 K was found which in turn corresponds to an activation volume corresponding to a sphere with D = 16 nm, close to the average physical volume of the particles [66,67]. Overall, the VSM measurements point out that particle reversal occurs by homogeneous rotation in single particles and not in large aggregated assemblies.

The TGA profiles of NPs@HNT and pristine HNT are presented in Fig. S6 (Suppl. Data). Three distinct thermal effects were observed in the curves of both samples, followed by the corresponding DTG peaks at approx. 60–70 °C, 250–290 °C and 490–500 °C (Insert – Fig. S6). For the first thermal effect and up to 200 °C – attributed to the loss of physisorbed water – the increased weight loss observed for pure HNTs compared to their magnetite containing counterparts is expected, considering that the NPs@HNT sample has already been treated at 200 °C during NPs synthesis. The second thermal effect, at around 250–300 °C is assigned to the loss of intercalated water [68] with similar weight loss observed for both NPs@HNT and pristine HNT samples. At higher temperatures, the weight loss observed for both samples at around 490–500 °C is characteristic for HNTs, and associated with the halloysite dehydroxylation, while for pure magnetite it has been documented that no weight loss occurs over 400 °C [69]. This difference in thermogravimetric behavior over 400 °C (11.81% loss for pure HNT and 8.73% for NPs@HNT, respectively) was employed to determine the magnetite content in NPs@HNT [30], which was found at 26% w/w.

3.2. Catalytic degradation of PCP

The kinetic results for the catalytic degradation of PCP in the presence of NPs@HNT in comparison to free, unsupported Fe_3O_4 (synthesized and evaluated for comparison purposes) are presented in Fig. 7. All results have been normalized per gram of the Fe_3O_4 containing phase. The overall kinetic results point out that the NPs@HNT hybrids can rapidly (i.e. within 30 min) degrade 10.2 mM of PCP/g of magnetite, at room temperature. In contrast, free, unsupported magnetite NPs exhibit much slower PCP degradation efficiency within the same time period i.e. ~3.5 mM/g of PCP were catalyzed in 30 min from free, unsupported Fe_3O_4 NPs. The free, unsupported NPs attain their maximum activity after 90 min reaching a maximum degradation efficiency of 5.6 mM PCP/g magnetite. Overall, the NPs@HNT hybrids achieve a 180% higher catalytic yield and 300% faster kinetics for PCP degradation. This behavior is mainly attributed to the better dispersion of the Fe_3O_4 NPs along the HNT nanotubes, therefore minimizing the inter-particle aggregation which is known to significantly hinder fast and efficient catalytic kinetics. On the contrary, the self-supported iron oxide NPs are highly aggregated, thus imposing two inhibitory factors in the catalytic process: [i] lower surface area of free NPs exposed to the solvent, [ii] diffusion barriers within the inter-particle voids. The development of iron oxide NPs attached at the HNT's surface minimizes both inhibitory factors, and this is evidenced as faster and more efficient catalytic degradation of PCP.

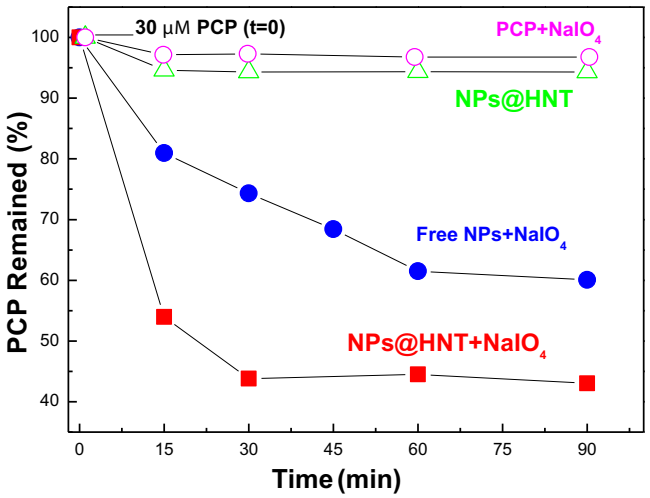

Fig. 7. Catalytic decomposition of 30 μM of PCP by the NPs@HNT hybrids (red squares) and the free NPs (blue circles). Control experiments: control sorption experiment performed without $NaIO_4$ [oxidant, Green triangles] and control experiment performed in the presence of $NaIO_4$ [oxidant] but without NPs (Purple circles). All results have been normalized for the same mass of Fe_3O_4 containing phase. (For interpretation of the references to colour in this figure legend, the reader is referred to the web version of this article.)

In principal, the oxidative catalytic decomposition of PCP by the NPs@HNT/$NaIO_4$ system is attributed to the well-studied mechanism that involves the decomposition of PCP at Fe-containing centers [8,9]. In particular, IO_4^- acts as an oxidant for the Fe-rich sites [70]. The iron atoms at the NP's surface can be oxidized via an 2-electron process forming either Fe^{4+} or Fe^{5+} species which in turn act as active catalytic sites for PCP decomposition. This mechanism is highly efficient for PCP decomposition via dechlorination and subsequent oxidative coupling between the formed products [8,9]. Additional control experiments were performed, in order to evaluate the adsorption of PCP by the NPs@HNT in absence of the oxidant ($NaIO_4$). Those measurements revealed only negligible (<0.200 mM/g) PCP adsorption per gram of Fe_3O_4 containing phase (Fig. 7, Green triangles), clearly supporting the role of the oxidant to the catalytic decomposition of PCP. In order to further highlight the catalytic decomposition activity of NPs@HNT hybrids, we performed additional control experiments. The results of those control experiments which were performed using PCP & $NaIO_4$ [oxidant] in the absence of NPs (Fig. 7, purple circles) revealed that the PCP decomposition was negligible. This finding clearly points-out that PCP degradation was negligible in the case where $NaIO_4$ was used alone in the absence of NPs@HNT hybrids. Overall, the catalytic data support that the removal of PCP from the reaction mixture is due to the catalytic decomposition of PCP by the NPs@HNT hybrids.

3.3. Catalyst reuse

After the first catalytic cycle, the hybrid NPs@HNT catalysts can be separated from the reaction mixture, by a facile recovery procedure involving the use of a magnet (Fig. 8, right). When the recovered materials were evaluated in a 2nd catalytic cycle (Fig. 8, black bars) nearly 91% of their initial catalytic activity was retained (after 90 min reaction), while even after their 4th catalytic cycle the NPs@HNT hybrids preserved 89% of their initial activity. On the contrary, the unsupported, free Fe_3O_4 NPs when evaluated under the same experimental conditions not only exhibited significantly lower catalytic efficiency but also lost their catalytic efficiency far more rapidly. In particular, free NPs (Fig. 8, red bars) retain less than 17% of their initial catalytic activity already from their 2nd catalytic cycle, while after their 4th catalytic cycle only a minor (<5% compared to initial value) activity was recorded. A possible explanation of the observed rapid deactivation of the unsupported Fe_3O_4 NPs can be attributed to blockage of the internal nanovoids of the aggregated self-supported particles after the first PCP decomposition cycle. This blockage is evidenced by the severe inhibition of PCP adsorption after the first reuse of the free Fe_3O_4 NPs and further confirmed by SEM images (Fig. S8). On the contrary, for the NPs@HNT hybrids the NPs dispersed along the HNT surface retain their PCP adsorption capacity after their reuse. It has been previously demonstrated that catalytic decomposition of PCP by iron-catalysts occurs via formation of polymeric species [8,9]. Within this context, the formation of those polymeric species is followed by formation of by-products which in turn can critically contribute to the clogging of the nanovoids in the case of free, unsupported Fe_3O_4 NPs. The proposed deactivation of unsupported NPs is in full agreement with previous studies on catalytic oxidation of 4-chlorophenol by magnetic Fe_3O_4 nanoparticles [71], according to which the free self-supported nanoparticles aggregated during reaction, forming larger, catalytically inactive flakes. However in our study, the use of HNTs hindered the formation of large assemblies (as discussed earlier) and enabled the NPs to retain their activity within multiple catalytic cycles.

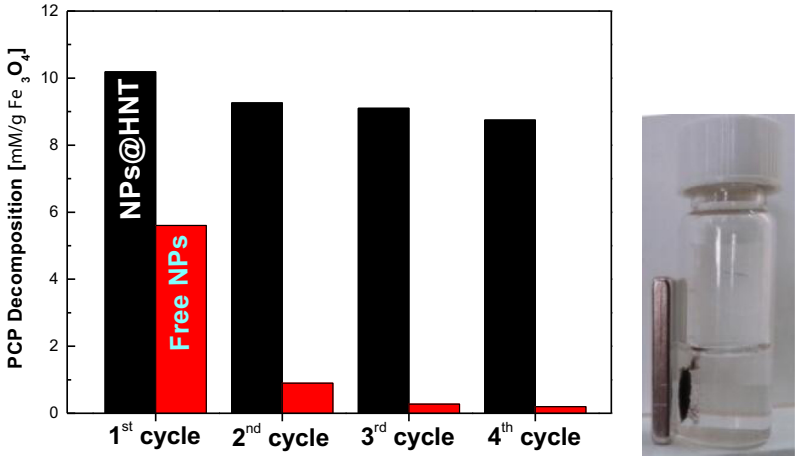

Fig. 8. Re-usability of NPs@HNT hybrids (black bars) and free NPs (red bars) for decomposition of PCP after multiple catalytic cycles (all results are for 90 min reaction duration). The photo at the right exemplifies the collection of the hybrids after the end of a catalytic cycle using a simple commercial magnet.

4. Conclusions

We demonstrated, a novel approach involving a modified wet-impregnation method for the *in situ* synthesis of small magnetite NPs at the surface of natural halloysite clay nanotubes. The reported approach is "green" in terms of synthesis, since we employed a natural occurring, highly abundant mineral (halloysite clay) as support but did not involve the use of any chemical reducing agent known to be toxic, harmful for the environment and unsafe to use. The thermal stability of the aluminosilicate HNT nanotubes and the interactions between the NPs precursor and HNT, render this unique one-dimensional clay mineral ideal support for the development of NPs upon thermal treatment in inert atmosphere. Due to being "naked", the NPs exhibited excellent catalytic activity towards the rapid degradation of PCP from reaction solutions at room temperature. The hybrids exhibit much higher catalytic efficiency and kinetics, compared to free unsupported magnetite NPs synthesized by alternative synthetic routes (e.g. co-precipitation method). Moreover, the hybrids are very promising in terms of reusability, since we demonstrated that they can be easily separated, cleaned and re-used for multiple catalytic cycles without any significant loss in their catalytic activity.

Acknowledgements

The authors would like to acknowledge the Laboratory Network of University of Ioannina for access to XPS measurements and in particular the Laser Facility group (Prof. Dr. G. Evangelakis, Head of group) of Physics Department. This research did not receive any specific grant from funding agencies in the public, commercial, or not-for-profit sectors.

Appendix A. Supplementary data

Supplementary data associated with this article can be found, in the online version, at http://dx.doi.org/10.1016/j.cej.2016.12.056.

References

[1] W.O. Yah, A. Takahara, Y.M. Lvov, Selective modification of halloysite lumen with octadecylphosphonic acid: new inorganic tubular micelle, J. Am. Chem. Soc. 134 (2012) 1853–1859.
[2] E. Joussein, S. Petit, J. Churchman, B. Theng, D. Righi, B. Delvaux, Halloysite clay minerals – a review, Clay Min. 40 (2005) 383–426.
[3] Y.M. Lvov, D.G. Shchukin, H. Möhwald, R.R. Price, Halloysite clay nanotubes for controlled release of protective agents, ACS Nano 2 (2008) 814–820.
[4] Y. Zhang, R. Gao, M. Liu, C. Yan, A. Shan, Adsorption of modified halloysite nanotubes in vitro and the protective effect in rats exposed to zearalenone, Arch. Anim. Nutr. 68 (2014) 320–335.
[5] V. Vergaro, E. Abdullayev, Y.M. Lvov, A. Zeitoun, R. Cingolani, R. Rinaldi, S. Leporatti, Cytocompatibility and uptake of halloysite clay nanotubes, Biomacromolecules 11 (2010) 820–826.
[6] L. Wang, J. Chen, L. Ge, V. Rudolph, Z. Zhu, Halloysite nanotube supported Ru nanocatalysts synthesized by the inclusion of preformed Ru nanoparticles for preferential oxidation of CO in H_2-rich atmosphere, J. Phys. Chem. C 117 (2013) 4141–4151.
[7] Y. Zhang, X. He, J. Ouyang, H. Yang, Palladium nanoparticles deposited on silanized halloysite nanotubes: synthesis, characterization and enhanced catalytic property, Sci. Rep. 3 (2013) 2948.
[8] K.C. Christoforidis, M. Louloudi, E.R. Milaeva, Y. Deligiannakis, Mechanism of catalytic decomposition of pentachlorophenol by a highly recyclable heterogeneous SiO_2-[Fe-porphyrin] catalyst, J. Catal. 270 (2010) 153–162.
[9] K.C. Christoforidis, M. Louloudi, Y. Deligiannakis, Complete dechlorination of pentachlorophenol by a heterogeneous SiO2-Fe-porphyrin catalyst, Appl. Catal. B Environ. 95 (2010) 297–302.
[10] A.P. Khodadoust, M.T. Suidan, G.A. Sorial, D.D. Dionysiou, R.C. Brenner, Desorption of Pentachlorophenol from Soils Using Mixed Solvents, Environ. Sci. Technol. 33 (1999) 4483–4491.
[11] B. Subramanian, V. Namboodiri, A.P. Khodadoust, D.D. Dionysiou, Extraction of pentachlorophenol from soils using environmentally benign lactic acid solutions, J. Hazard. Mater. 174 (2010) 263–269.
[12] P.R. Cooke, J.R. Lindsay Smith, Alkene epoxidation catalysed by ligand-bound supported metalloporphyrins, Tetrahedron Lett. 33 (1992) 2737–2740.
[13] A.H. Lu, E.L. Salabas, F. Schüth, Magnetic nanoparticles: synthesis, protection, functionalization, and application, Angew. Chem. Int. Ed. 46 (2007) 1222–1244.
[14] L. Xu, J. Wang, Fenton-like degradation of 2,4-dichlorophenol using Fe_3O_4 magnetic nanoparticles, Appl. Catal. B Environ. 123 (2012) 117–126.
[15] X. Xue, K. Hanna, M. Abdelmoula, N. Deng, Adsorption and oxidation of PCP on the surface of magnetite: kinetic experiments and spectroscopic investigations, Appl. Catal. B. Environ. 89 (2009) 432–440.
[16] D. Brondani, C.W. Scheeren, J. Dupont, I.C. Vieira, Halloysite clay nanotubes and platinum nanoparticles dispersed in ionic liquid applied in the development of a catecholamine biosensor, Analyst 137 (2012) 3732–3739.
[17] H. Zhu, M. Du, M. Zou, C. Xu, Y. Fu, Green synthesis of Au nanoparticles immobilized on halloysite nanotubes for surface-enhanced Raman scattering substrates, Dalton Trans. 41 (2012) 10465–10471.
[18] B.J. Sanghavi, G. Hirsch, S.P. Karna, A.K. Srivastava, Potentiometric stripping analysis of methyl and ethyl parathion employing carbon nanoparticles and halloysite nanoclay modified carbon paste electrode, Anal. Chim. Acta 735 (2012) 37–45.
[19] H. Cao, X. Sun, Y. Zhang, N. Jia, Electrochemical sensing based on gold nanoparticle-decorated halloysite nanotube composites, Anal. Biochem. 430 (2012) 111–115.
[20] X. Tang, L. Li, B. Shen, C. Wang, Halloysite-nanotubes supported FeNi alloy nanoparticles for catalytic decomposition of toxic phosphine gas into yellow phosphorus and hydrogen, Chemosphere 91 (2013) 1368–1373.
[21] P. Wang, M. Du, M. Zhang, H. Zhu, S. Bao, M. Zou, T. Yang, Facile fabrication of AuNPs/PANI/HNTs nanostructures for high-performance electrochemical sensors towards hydrogen peroxide, Chem. Eng. J. 248 (2014) 307–314.
[22] P. Liu, M. Zhao, Silver nanoparticle supported on halloysite nanotubes catalyzed reduction of 4-nitrophenol, Appl. Surf. Sci. 255 (2009) 3989–3993.
[23] E. Abdullayev, R. Price, D. Shchukin, Y. Lvov, Halloysite tubes as nanocontainers for anticorrosion coating with benzotriazole, ACS Appl. Mater. Interfaces 1 (2009) 1437–1443.
[24] X. Shi, T.A. Nguyen, Z. Suo, Y. Liu, R. Avci, Effect of nanoparticles on the anticorrosion and mechanical properties of epoxy coating, Surf. Coat. Technol. 204 (2009) 237–245.
[25] Y. Zhang, Y. Chen, H. Zhang, B. Zhang, J. Liu, Potent antibacterial activity of a novel silver nanoparticle-halloysite nanotube nanocomposite powder, J. Inorg. Biochem. 118 (2013) 59–64.
[26] C. Li, X. Li, X. Duan, G. Li, J. Wang, Halloysite nanotube supported Ag nanoparticles heteroarchitectures as catalysts for polymerization of alkylsilanes to superhydrophobic silanol/siloxane composite microspheres, J. Colloid Interface Sci. 436 (2014) 70–76.
[27] X. Ding, H. Wang, W. Chen, J. Liu, Y. Zhang, Preparation and antibacterial activity of copper nanoparticle/halloysite nanotube nanocomposites via reverse atom transfer radical polymerization, RCS Adv. 4 (2014) 41993–41996.
[28] S. Zhong, C. Zhou, X. Zhang, H. Zhou, H. Li, X. Zhu, Y. Wang, A novel molecularly imprinted material based on magnetic halloysite nanotubes for rapid enrichment of 2,4-dichlorophenoxyacetic acid in water, J. Hazard. Mater. 276 (2014) 58–65.
[29] X. Tian, W. Wang, N. Tian, C. Zhou, C. Yang, S. Komarneni, Cr(VI) reduction and immobilization by novel carbonaceous modified magnetic Fe3O4/halloysite nanohybrid, J. Hazard. Mater. 309 (2016) 151–156.
[30] Y. Xie, D. Qian, D. Wu, X. Ma, Magnetic halloysite nanotubes/iron oxide composites for the adsorption of dyes, Chem. Eng. J. 168 (2011) 959–963.
[31] S. Yang, P. Zong, J. Hu, G. Sheng, Q. Wang, X. Wang, Fabrication of β-cyclodextrin conjugated magnetic HNT/iron oxide composite for high-efficient decontamination of U(VI), Chem. Eng. J. 214 (2013) 376–385.
[32] O. Owoseni, E. Nyankson, Y. Zhang, D.J. Adams, J. He, L. Spinu, G.L. McPherson, A. Bose, R.B. Gupta, V.T. John, Interfacial adsorption and surfactant release characteristics of magnetically functionalized halloysite nanotubes for responsive emulsions, J. Colloid Interface Sci. 463 (2016) 288–298.
[33] S. Laurent, D. Forge, M. Port, A. Roch, C. Robic, L. Vander Elst, R.N. Muller, Magnetic iron oxide nanoparticles: Synthesis, stabilization, vectorization, physicochemical characterizations and biological applications, Chem. Rev. 108 (2008) 2064–2110.
[34] Cancer Theranostics, Academic Press, 2014.
[35] Y. Zhao, E. Abdullayev, A. Vasiliev, Y. Lvov, Halloysite nanotubule clay for efficient water purification, J. Colloid Interface Sci. 406 (2013) 121–129.
[36] T. Tsoufis, Z. Syrgiannis, N. Akhtar, M. Prato, F. Katsaros, Z. Sideratou, A. Kouloumpis, D. Gournis, P. Rudolf, In situ growth of capping-free magnetic iron oxide nanoparticles on liquid-phase exfoliated graphene, Nanoscale 7 (2015) 8995–9003.
[37] T. Tsoufis, A.P. Douvalis, C.E. Lekka, P.N. Trikalitis, T. Bakas, D. Gournis, Controlled preparation of carbon nanotube-iron oxide nanoparticle hybrid materials by a modified wet impregnation method, J. Nanopart. Res. 15 (2013) 1924.
[38] M.A. Karakassides, D. Gournis, A.B. Bourlinos, P.N. Trikalitis, T. Bakas, Magnetic Fe_2O_3-Al_2O_3 composites prepared by a modified wet impregnation method, J. Mater. Chem. 13 (2003) 871–876.
[39] M. Baikousi, A.B. Bourlinos, A. Douvalis, T. Bakas, D.F. Anagnostopoulos, J. Tuček, K. Šafářová, R. Zboril, M.A. Karakassides, Synthesis and characterization of γ-Fe_2O_3/carbon hybrids and their application in removal of hexavalent chromium ions from aqueous solutions, Langmuir 28 (2012) 3918–3930.
[40] W.O. Yah, H. Xu, H. Soejima, W. Ma, Y. Lvov, A. Takahara, Biomimetic dopamine derivative for selective polymer modification of halloysite nanotube lumen, J. Am. Chem. Soc. 134 (2012) 12134–12137.

[41] A.B. Bourlinos, M.A. Karakassides, A. Simopoulos, D. Petridis, Synthesis and characterization of magnetically modified clay composites, Chem. Mater. 12 (2000) 2640–2645.
[42] S.K. Papageorgiou, E.P. Kouvelos, E.P. Favvas, A.A. Sapalidis, G.E. Romanos, F.K. Katsaros, Metal-carboxylate interactions in metal-alginate complexes studied with FTIR spectroscopy, Carbohydr. Res. 345 (2010) 469–473.
[43] Y. Tian, B. Yu, X. Li, K. Li, Facile solvothermal synthesis of monodisperse Fe_3O_4 nanocrystals with precise size control of one nanometre as potential MRI contrast agents, J. Mater. Chem. 21 (2011) 2476–2481.
[44] V. Chandra, J. Park, Y. Chun, J.W. Lee, I.C. Hwang, K.S. Kim, Water-dispersible magnetite-reduced graphene oxide composites for arsenic removal, ACS Nano 4 (2010) 3979–3986.
[45] V. Abbasov, T. Mammadova, N. Andrushenko, N. Hasankhanova, Y. Lvov, E. Abdullayev, Halloysite-Y-zeolite blends as novel mesoporous catalysts for the cracking of waste vegetable oils with vacuum gasoil, Fuel 117 (2014) 552–555.
[46] H. Lun, J. Ouyang, H. Yang, Natural halloysite nanotubes modified as an aspirin carrier, RSC Advances 4 (2014) 44197–44202.
[47] E. Abdullayev, A. Joshi, W. Wei, Y. Zhao, Y. Lvov, Enlargement of halloysite clay nanotube lumen by selective etching of aluminum oxide, ACS Nano 6 (2012) 7216–7226.
[48] D.G. Shchukin, G.B. Sukhorukov, R.R. Price, Y.M. Lvov, Halloysite nanotubes as biomimetic nanoreactors, Small 1 (2005) 510–513.
[49] Y. Joo, J.H. Sim, Y. Jeon, S.U. Lee, D. Sohn, Opening and blocking the inner-pores of halloysite, Chem. Commun. 49 (2013) 4519–4521.
[50] S. Mellouk, A. Belhakem, K. Marouf-Khelifa, J. Schott, A. Khelifa, Cu(II) adsorption by halloysites intercalated with sodium acetate, J. Colloid Interface Sci. 360 (2011) 716–724.
[51] M. Kleber, L. Schwendenmann, E. Veldkamp, J. Rößner, R. Jahn, Halloysite versus gibbsite: Silicon cycling as a pedogenetic process in two lowland neotropical rain forest soils of La Selva, Costa Rica, Geoderma 138 (2007) 1–11.
[52] P. Yuan, P.D. Southon, Z. Liu, M.E.R. Green, J.M. Hook, S.J. Antill, C.J. Kepert, Functionalization of halloysite clay nanotubes by grafting with γ-aminopropyltriethoxysilane, J. Phys. Chem. C 112 (2008) 15742–15751.
[53] O.A. Chadwick, G.H. Brimhall, D.M. Hendricks, From a black to a gray box – a mass balance interpretation of pedogenesis, Geomorphology 3 (1990) 369–390.
[54] K. Kardimi, T. Tsoufis, A. Tomou, B.J. Kooi, M.I. Prodromidis, D. Gournis, Synthesis and characterization of carbon nanotubes decorated with Pt and PtRu nanoparticles and assessment of their electrocatalytic performance, Int. J. Hydrogen Energy 37 (2012) 1243–1253.
[55] T. Tsoufis, A. Tomou, D. Gournis, A.P. Douvalis, I. Panagiotopoulos, B. Kooi, V. Georgakilas, I. Arfaoui, T. Bakas, Novel nanohybrids derived from the attachment of FePt nanoparticles on carbon nanotubes, J. Nanosci. Nanotechnol. 8 (2008) 5942–5951.
[56] T. Fujii, F.M.F. De Groot, G.A. Sawatzky, F.C. Voogt, T. Hibma, K. Okada, In situ XPS analysis of various iron oxide films grown by NO_2-assisted molecular-beam epitaxy, Phys. Rev. B 59 (1999) 3195–3202.
[57] L. Jian, J. Xiuling, C. Dairong, L. Wei, Solvothermal synthesis and characterization of Fe_3O_4 and γ-Fe_2O_3 nanoplates, J. Phys. Chem. C 113 (2009) 4012–4017.
[58] V. Papaefthimiou, I. Florea, W. Baaziz, I. Janowska, W.H. Doh, D. Begin, R. Blume, A. Knop-Gericke, O. Ersen, C. Pham-Huu, S. Zafeiratos, Effect of the specific surface sites on the reducibility of α-Fe_2O_3/graphene composites by hydrogen, J. Phys. Chem. C 117 (2013) 20313–20319.
[59] M. Descostes, F. Mercier, N. Thromat, C. Beaucaire, M. Gautier-Soyer, Use of XPS in the determination of chemical environment and oxidation state of iron and sulfur samples: constitution of a data basis in binding energies for Fe and S reference compounds and applications to the evidence of surface species of an oxidized pyrite in a carbonate medium, Appl. Surf. Sci. 165 (2000) 288–302.
[60] A.L. Morel, S.I. Nikitenko, K. Gionnet, A. Wattiaux, J. Lai-Kee-Him, C. Labrugere, B. Chevalier, G. Deleris, C. Petibois, A. Brisson, M. Simonoff, Sonochemical approach to the synthesis of Fe_3O_4@SiO_2 core–shell nanoparticles with tunable properties, ACS Nano 2 (2008) 847–856.
[61] X. Teng, D. Black, N.J. Watkins, Y. Gao, H. Yang, Platinum-maghemite core-shell nanoparticles using a sequential synthesis, Nano Lett. 3 (2003) 261–264.
[62] Y. Zhang, Y. Xie, A. Tang, Y. Zhou, J. Ouyang, H. Yang, Precious-metal nanoparticles anchored onto functionalized halloysite nanotubes, Ind. Eng. Chem. Res. 53 (2014) 5507–5514.
[63] A. Mekki, D. Holland, C.F. McConville, M. Salim, An XPS study of iron sodium silicate glass surfaces, J. Non-Cryst. Solids 208 (1996) 267–276.
[64] S.J. Park, S. Kim, S. Lee, Z.G. Khim, K. Char, T. Hyeon, Synthesis and magnetic studies of uniform iron nanorods and nanospheres, J. Am. Chem. Soc. 122 (2000) 8581–8582.
[65] A.G. Roca, M.P. Morales, K. O'Grady, C.J. Serna, Structural and magnetic properties of uniform magnetite nanoparticles prepared by high temperature decomposition of organic precursors, Nanotechnology 17 (2006) 2783–2788.
[66] A. Lyberatos, R.W. Chantrell, The fluctuation field of ferromagnetic materials, J. Phys. Condens. Matter 9 (1997) 2623–2643.
[67] V. Basso, C. Beatrice, M. LoBue, P. Tiberto, G. Bertotti, Connection between hysteresis and thermal relaxation in magnetic materials, Phys. Rev. B 61 (2000) 1278–1285.
[68] A.F. Ismail, S.A. Hashemifard, T. Matsuura, Facilitated transport effect of Ag^+ ion exchanged halloysite nanotubes on the performance of polyetherimide mixed matrix membrane for gas separation, J. Membr. Sci. 379 (2011) 378–385.
[69] J.P. Sanders, P.K. Gallagher, Kinetics of the oxidation of magnetite using simultaneous TG/DSC, J. Therm. Anal. Calorim. 72 (2003) 777–789.
[70] K.C. Christoforidis, M. Louloudi, E.R. Milaeva, Y. Sanakis, Y. Deligiannakis, EPR study of a novel [Fe-porphyrin] catalyst, Mol. Phys. 105 (2007) 2185–2194.
[71] R. Cheng, G.Q. Li, C. Cheng, L. Shi, X. Zheng, Z. Ma, Catalytic oxidation of 4-chlorophenol with magnetic Fe_3O_4 nanoparticles: mechanisms and particle transformation, RSC Adv 5 (2015) 66927–66933.